Research Square

Preprints are preliminary reports that have not undergone peer review.
They should not be considered conclusive, used to inform clinical practice,
or referenced by the media as validated information.

Multidimensional EEG Representations and Classification of Grip- Force-Level Motor Imagery

Yan Bian

aileanbian@hotmail.com

Tianjin University of Technology and Education

Zhao Jialing

Tianjin University of Technology and Education

Tian Linqing

Tianjin University of Technology and Education

Yu Xinting

Tianjin University of Technology and Education

Jian Dong

Tianjin University of Technology and Education

Research Article

Keywords: motor imagery, grip-force level, deep learning, directed functional connectivity, brain–computer interface

Posted Date: August 5th, 2026

DOI: https://doi.org/10.21203/rs.3.rs-10454191/v1

License: This work is licensed under a Creative Commons Attribution 4.0 International License.
Read Full License

Additional Declarations: No competing interests reported.

Full Length Article

Multidimensional EEG Representations and Classification of Grip-Force-Level Motor Imagery

Yan Bian*, Zhao Jialing, Tian Linqing, Yu Xinting,Jian Dong

Tianjin Key Laboratory of Information Sensing and Intelligent Control, Tianjin University of Technology and Education, Tianjin, China

* Corresponding author.

E-mail address: aileanbian@hotmail.com; 2649448484@qq.com; 2694908409@qq.com;2425268799@qq.com;dongjian2007.happy@163.com

Abstract

Existing motor imagery brain–computer interfaces mainly discriminate coarse-grained movement categories, such as left-hand, right-hand, and foot movements, and therefore have limited ability to represent graded grip-force intentions during hand rehabilitation. To characterize the neural representations and decodability of motor imagery at different grip-force levels, 12 healthy participants performed a motor execution–guided motor imagery task under 10%, 50%, and 90% of maximum voluntary contraction. Movement-related cortical potentials, event-related spectral perturbations, and the directed phase lag index were used to examine time-domain, time–frequency, and directional functional connectivity features across force conditions. The classification performance of EEGSym was compared with that of FBCSP-SVM, FBCSP-MDM, and a probability-weighted fusion model. The results showed a significant condition effect in the movement-related cortical potential at C4, more pronounced beta-band event-related desynchronization over the central sensorimotor region under the high-force condition, and significant differences in directional functional networks in the delta, alpha, and gamma bands. EEGSym achieved the highest classification accuracy among the compared models. Its accuracies for low-versus-high and medium-versus-high force classification were 77.81% ± 18.90% and 72.60% ± 15.23%, respectively,

while the three-class accuracy reached 62.01% ± 21.82%. All of these tasks performed significantly above their corresponding theoretical chance levels. These findings indicate that motor imagery at different force levels produces distinguishable neural representations across slow cortical potentials, sensorimotor rhythms, and directional functional networks. EEGSym can effectively capture spatiotemporal features associated with subtle force differences, providing a basis for decoding force-graded motor intentions in rehabilitation robots, intelligent prostheses, and biomimetic robotic hands.
Keywords: motor imagery; grip-force level; deep learning; directed functional connectivity; brain–computer interface.

0.Introduction

Brain–computer interfaces (BCIs) establish a direct communication pathway between the brain and external devices, providing a new technological approach for restoring motor function in patients with stroke, spinal cord injury, and other motor impairments (Ma et al., 2024; Yu et al., 2025). Among the various BCI paradigms, motor imagery (MI)-based BCIs are non-invasive, easy to implement, and capable of promoting active patient engagement, making them an important research direction in neurorehabilitation (Yu et al., 2025). Most existing MI-BCI studies focus on relatively coarse motor categories, such as left-hand, right-hand, foot, or tongue movements, and therefore cannot adequately capture intentions to regulate grip force during rehabilitation. In hand rehabilitation, grasping involves not only movement type but also motor parameters such as force magnitude, duration, and fine motor control. When an external device provides fixed feedback based solely on movement category, the intended grip force, sensory feedback, and device response may become mismatched, potentially reducing the effectiveness of neurofeedback training (Ma et al., 2024; Yu et al., 2025). Therefore, decoding grip-force levels from MI-related EEG may enable rehabilitation robots, intelligent prostheses, and biomimetic robotic hands to provide feedback that more closely matches the user's grip-force intention during functional activities such as grasping, holding objects, and fine hand manipulation (Chen et al., 2026; Jochumsen et al., 2017; Karakullukcu et al., 2024; Li et al., 2023; Li et al., 2024; Rong et al., 2024; Saibene et al., 2023; Sheng et al., 2023; Sun et al., 2025; Wang et al., 2017).

Previous studies have made preliminary attempts to decode fine hand movements and grip-force intentions. Li et al. (2024) investigated six classes of executed fine hand movements, including five-finger closure, index-finger extension, and thumb extension performed with the left or right hand. A convolutional neural network (CNN) was used to decode motor-execution electroencephalography (EEG) signals, achieving a mean classification accuracy of 79.20%±6.05% across 10 participants. Jochumsen et al. (2017) combined EEG rhythm features with movement-

related cortical potentials (MRCPs) to perform single-trial classification of grasp types and force–speed combinations. The mean accuracy for classifying palmar grasp, lateral grasp, and pinch grasp was 48%±5%. The four-class force–speed task comprised rapidly reaching 20% maximum voluntary contraction (MVC), rapidly reaching 60% MVC, slowly reaching 20% MVC, and slowly reaching 60% MVC, where the rapid and slow conditions required the target force to be reached within 0.5 and 3 s, respectively. The mean four-class accuracy during MI was 39%±8%. Wang et al. (2017) designed right-hand grasp imagery tasks at 10% and 30% MVC and used multi-band common spatial pattern (Multi-CSP) features and a support vector machine (SVM) to distinguish low-force imagery, high-force imagery, and rest, achieving a mean online classification accuracy of 70.9%. Li et al. (2023) investigated right-hand isometric grip imagery at 5% and 40% MVC and used common spatial pattern (CSP) features, EEG coherence features, and an SVM for single-trial discrimination of the two grip-force intentions, obtaining an online binary classification accuracy of 76.67%±9.35%. Karakullukcu et al. (2024) conducted motor execution and MI experiments involving light, medium, and heavy object weights and extracted EEG features using the Fourier-based synchrosqueezing transform (FSST) and regularized common spatial pattern (RCSP). The mean pairwise classification accuracy exceeded 70% for all weight combinations, although performance varied across comparisons, indicating that different weight levels were distinguishable. Chen et al. (2026) further compared actual gripping at 20% and 100% MVC and used EEG functional-connectivity features to classify grip-force levels during motor planning, achieving a mean accuracy of 75.58%±14.68%. These findings indicate that EEG activity related to the anticipated grip-force level emerges before the onset of actual gripping; however, the reliable extraction and accurate decoding of such information remain challenging.

Beyond classification performance, the neurophysiological representations underlying different grip-force levels during MI remain insufficiently understood. Existing studies have generally focused on a single type of EEG feature, such as event-related

desynchronization/synchronization (ERD/ERS) of sensorimotor rhythms (Zhao et al., 2018) or time-domain MRCP features (Shibasaki & Hallett, 2006). However, grip-force-level MI involves multiple neural processes, including motor preparation, maintenance of motor representations, and coordination within sensorimotor networks. MRCPs reflect slow cortical potential changes associated with motor preparation and planning (Shibasaki & Hallett, 2006), whereas ERD/ERS characterizes changes in the synchronization of sensorimotor cortical rhythms (Zhao et al., 2018). Functional connectivity can further be used to characterize phase relationships and coordination patterns among distributed brain regions (Stam et al., 2007). Although EEG dynamics during the execution and imagery of different grip forces have been investigated using microstate analysis (Fu et al., 2018), the topology and spatial distribution of whole-brain directed functional connectivity under different grip-force conditions have not been systematically examined. Therefore, analyses based on a single feature domain may be insufficient to fully characterize the neural differences associated with grip-force-level MI, highlighting the need for an integrated investigation across the time, time–frequency, and functional-connectivity domains.

Neural differences between adjacent grip-force levels are relatively subtle, whereas EEG signals have a low signal-to-noise ratio, pronounced inter-individual variability, and non-stationarity. Consequently, conventional handcrafted features may not adequately capture their dynamic spatiotemporal characteristics. In addition, conventional channel arrangements do not fully exploit the spatial correspondence between electrodes over the left and right hemispheres during hand MI. To address these issues, the present study established three grip-force conditions corresponding to 10%, 50%, and 90% MVC. MRCPs, event-related spectral perturbations (ERSPs), and the directed phase lag index (dPLI) were used to characterize EEG responses at different grip-force levels from the time-domain, time–frequency, and directed functional-network perspectives, respectively. For classification, the EEGSym network (Pérez-Velasco et al., 2022) reconstructed the spatial correspondence between symmetrical electrodes over the two hemispheres and jointly learned

multiscale spatiotemporal features, thereby improving the model's ability to distinguish subtle differences in grip-force level. A conventional machine-learning baseline based on filter bank common spatial pattern (FBCSP) features was also constructed. Class-probability outputs were obtained using an SVM and a Riemannian minimum distance to mean (MDM) classifier (Barachant et al., 2012; Li et al., 2023; Pan et al., 2025; Wang et al., 2017) and then combined through probability-weighted decision fusion. To evaluate the contribution of the fusion strategy, separate FBCSP-SVM and FBCSP-MDM single-branch models were included as comparison models. Under a unified data-partitioning and evaluation framework, a three-class task involving low, medium, and high grip-force levels and three pairwise binary classification tasks were conducted to determine whether the three grip-force intentions could be decoded and to compare the classification difficulty of adjacent and nonadjacent grip-force levels. By combining neurophysiological characterization with classification experiments, this study further examined the neural responses and separability associated with grip-force-level MI.

1. Materials and Methods

1.1 Participants

Twelve university students were recruited for this study, including eight men and four women, aged 23–28 years. All participants were right-handed, had no history of neurological disorders, had not taken any medication that could affect mood or nervous system function within the week preceding the experiment, and had no prior experience with similar experimental tasks. Before the experiment, all participants were familiarized with the experimental procedure and provided written informed consent. The study was approved by the Ethics Committee of Tianjin University of Technology and Education (approval no. 2025-08).

1.2 Experimental Paradigm

The experiment was conducted in a sound-attenuated room under stable lighting conditions. EEG signals were recorded using a SynAmps2 amplifier and a 64-channel Ag/AgCl electrode cap.

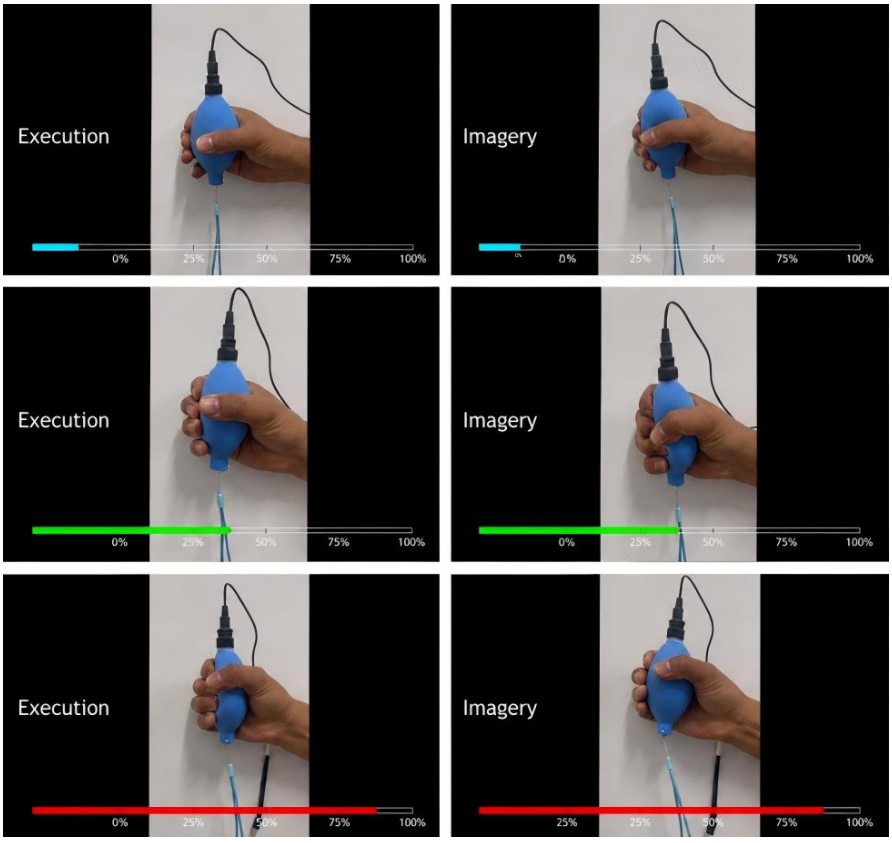
A right-hand grip-force task was employed. Before the experiment, the maximum voluntary contraction (MVC) of the right hand was measured for each participant using an electronic hand dynamometer, as shown in Fig. 1(a). Participants were instructed to exert their maximum grip force continuously for 5 s. Three measurements were obtained, with a 2-min interval between consecutive measurements to minimize the effects of muscular fatigue. The maximum value across the three measurements was used as the individual MVC reference. This participant-specific MVC calibration was performed to reduce bias arising from inter-individual differences in absolute grip strength. Based on previous studies (Karakullukcu et al., 2024; Wang et al., 2017), three grip-force conditions were defined: low (10% MVC), medium (50% MVC), and high (90% MVC), corresponding to grasping light objects, commonly used everyday objects, and relatively heavy objects, respectively.

Before the formal experiment, all participants completed a pretraining session to become familiar with the experimental procedure, visual cues, and the three target grip-force levels. During pretraining, participants practiced grasping at different grip-force levels under the guidance of the researchers and adjusted their actual force output according to feedback from the electronic hand dynamometer. They subsequently practiced the MI tasks corresponding to each grip-force level. The formal experiment commenced only after the participants had demonstrated that they understood the task requirements, could distinguish among the three grip-force levels, and could perform the motor execution and MI tasks according to the experimental cues.

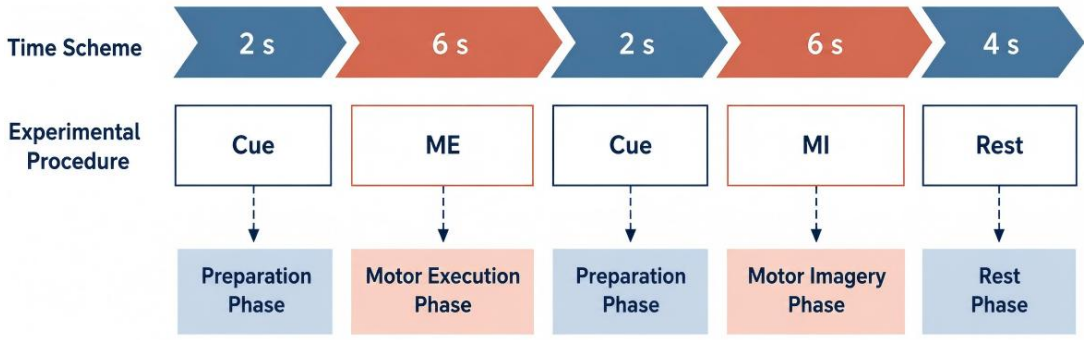
To help participants form MI corresponding to each target grip-force level, an ME-guided MI paradigm was adopted (Pérez-Velasco et al., 2025). In each trial, participants first executed a grasp at the target grip-force level to establish the corresponding kinesthetic and proprioceptive representations. They were then instructed to imagine gripping with the

right hand at the same grip-force level. A dynamic progress bar at the bottom of the screen indicated the target grip-force level for the current trial through its color and length, as illustrated in Fig. 1(a).

As shown in Fig. 1(b), each trial lasted 20 s. A 2s preparatory cue was first presented, followed by 6s of ME. After a second 2s preparatory cue, participants entered a 6s MI period, during which they were instructed to imagine gripping with the right hand at the same grip-force level as in the preceding ME period while avoiding overt muscle contraction or limb movement. This was followed by a 4s rest period. Each run comprised 20 trials for each of the three conditions, yielding 60 trials in total. Each participant completed two runs, resulting in 120 trials, with the three conditions presented in a randomized order. A rest period of at least 5 min was provided between runs, and MVC was remeasured before each run to recalibrate potential fatigue-related changes in force output.



(a). Visual cue interface for the experimental task



(b). Single-trial timeline for grip-force-level motor execution and imagery

Fig. 1. Experimental paradigm and trial timeline for grip-force-level motor imagery

1.3 Data Preprocessing

Scalp EEG signals are weak physiological signals with amplitudes on the order of microvolts (μV) and are susceptible to contamination by electrooculographic (EOG) artifacts, electromyographic (EMG) activity, electrode-contact noise, and other interference during acquisition. To obtain EEG data with an adequate signal-to-noise ratio for subsequent multidimensional feature analysis, the raw continuous EEG recordings were preprocessed offline using MATLAB R2024b (MathWorks, USA) and the EEGLAB toolbox (v2021.1) (Delorme & Makeig, 2004).

The preprocessing procedure included EEG data import, removal of channels not used in the subsequent analyses (CB1, CB2, M1, M2, HEO, VEO, EMG1, and EMG2), electrode-location assignment, common average referencing, 0–75 Hz band-pass filtering, bad-channel interpolation, and rejection of contaminated data segments. Independent component analysis (ICA) was subsequently applied to remove ocular and muscular components from the EEG signals. This procedure served as the general preprocessing pipeline. Separate processing branches were then established for the MRCP, ERSP, dPLI, and classification analyses, with analysis-specific frequency-band filtering and feature-extraction parameters applied in each branch.

1.4 Neurophysiological Feature Extraction and Network Analysis

1.4.1 MRCP Feature Extraction

MRCPs are low-frequency event-related potentials associated with motor preparation and task initiation and reflect slow cortical potential changes during the formation of motor intention. Their typical components include the readiness potential (RP), motor potential (MP), and movement-monitoring-related components. Unlike sensorimotor rhythms (SMRs), which primarily reflect rhythmic activity changes in the sensorimotor cortex, MRCPs are time-locked to task events and provide time-domain information related to motor intention (Shibasaki & Hallett, 2006).

Before MRCP feature extraction, the preprocessed EEG signals were filtered using a zero-phase finite impulse response (FIR) band-pass filter from 0.05 to 5 Hz. This filtering preserved slow potential components associated with motor preparation and motor imagery while attenuating low-frequency drift and high-frequency noise that could affect MRCP waveform estimation. The onset of the MI cue was defined as the temporal reference point (t=0ms), and channels C3, Cz, and C4 were selected for analysis. For the right-hand task, C3 primarily corresponds to the contralateral sensorimotor cortex, C4 to the ipsilateral sensorimotor cortex, and Cz to the central midline region.

Let $x_{s,c,k,r}(t)$ denote the MRCP signal from the r-th valid trial of participant s, under grip-force condition c, and at channel k, where $k \in C3, Cz, C4$ .Baseline correction was first applied to each trial. Subsequently, all valid trials were averaged within each participant, grip-force condition, and channel to obtain the participant-level mean MRCP waveform:

$$\bar{x}_{s,c,k}(t) = \frac{1}{N_{s,c}} \sum_{r=1}^{N_{s,c}} x_{s,c,k,r}(t) \tag{1}$$

Where $N_{s,c}$ denotes the number of valid trials for participant s under grip-force condition c .The Early RP mean amplitude, negative slope (NS) mean amplitude, MP peak amplitude, and MP latency were then extracted from the participant-level mean waveform for each participant, condition,

and channel. These participant-level features served as the statistical units for the subsequent repeated-measures analysis of variance.

The following time-domain measures were extracted from the participant-level mean MRCP waveform: $\bar{x}_{s,c,k}(t)$

(1) Early RP: The interval from −1500 to −500 ms was selected, and the mean amplitude of the participant-level mean MRCP waveform within this interval was calculated.

(2) Late RP / NS: The interval from −500 to −150 ms was selected, and the mean amplitude of the participant-level mean MRCP waveform within this interval was calculated.

(3) MP: The interval from −150 to 1000 ms was selected as the analysis window. The most negative peak, corresponding to the minimum voltage of the participant-level mean MRCP waveform, was identified within this interval, and its latency was recorded.

Accordingly, the Early RP mean amplitude, NS mean amplitude, MP peak amplitude, and MP latency were obtained for each participant under each grip-force condition and at each channel of interest and were subsequently used for group-level statistical analysis.

1.4.2 ERSP Analysis

To characterize dynamic changes in EEG spectral power during ME-guided MI, event-related spectral perturbation (ERSP) analysis was used to quantify event-related desynchronization and synchronization (ERD/ERS). MRCPs primarily reflect phase-locked time-domain activity, whereas ERSPs characterize non-phase-locked changes in time–frequency power. Thus, these measures describe movement-related neural activity from complementary time-domain and time–frequency perspectives, respectively (Zhao et al., 2018).

ERSPs were calculated using the short-time Fourier transform (STFT).Let $X_{i,c}(t,f)$ denote the complex STFT coefficient of the i-th trial at channel c, time t, and frequency f. The corresponding instantaneous spectral power was calculated as:

$$P_{i,c}(t,f)=|X_{i,c}(t,f)|^2 \quad (2)$$

To reduce the influence of inter-participant and inter-channel differences in background EEG power, the onset of the MI cue was defined

as t=0 s, and the EEG data were segmented from −2 to 7 s relative to cue onset. The interval from −2000 to −1500 ms before the MI cue was selected as the baseline period. The baseline power of the *i*-th trial at frequency *f* was defined as:

$$P_{i,c}^{base}(f)=\frac{1}{|B|}\sum_{\tau \in B} P_{i,c}(\tau,f) \tag{3}$$

Where B denotes the baseline interval and |B|represents the number of time points within the baseline interval. Baseline correction was subsequently performed in decibels:

$$ERSP_{i,c}(t,f)=10\,log_{10}\left[\frac{P_{i,c}(t,f)}{P_{i,c}^{base}(f)}\right] \tag{4}$$

The ERSPs of the N trials under the same condition were then averaged to obtain the condition-level ERSP:

$$\overline{ERSP_c}(t,f)=\frac{1}{N}\sum_{i=1}^{N} ERSP_{i,c}(t,f) \tag{5}$$

After baseline correction, negative ERSP values indicate event-related desynchronization (ERD), whereas positive values indicate event-related synchronization (ERS).

1.4.3 Directed Functional Brain Network Construction

To characterize directed functional connectivity among brain regions under different grip-force conditions, directed functional brain networks were constructed using the directed phase lag index (dPLI). Compared with undirected measures such as coherence and the phase-locking value (PLV), the phase lag index (PLI) reduces, to some extent, the effects of zero-phase synchronization and volume conduction on functional connectivity estimation (Stam et al., 2007). Based on PLI, dPLI further quantifies phase-leading and phase-lagging relationships between channels (Stam & van Straaten, 2012).

Network nodes were selected by taking the union of the electrodes ranked within the top 10% in terms of both in-degree and out-degree under each task condition, resulting in 52 key electrodes. The preprocessed EEG signals were first filtered using zero-phase band-pass filters in five frequency bands: Delta (0.5–4 Hz), Theta (4–8 Hz), Alpha (8–13 Hz), Beta (13–30 Hz), and Gamma (30–50 Hz). The instantaneous phase of each channel was then extracted using the Hilbert transform. For the signal

$x_i(t)$,from channel i, its analytic signal was expressed as:

$$Z_i(t)=x_i(t)+j\tilde{x}_i(t)=A_i(t)e^{i\emptyset_i(t)} \quad (6)$$

where $\tilde{x}_i(t)$ denotes the Hilbert transform of the original signal,$A_i(t)$is the instantaneous amplitude,and $\emptyset_i(t)$ is the instantaneous phase. The phase difference between channels i and j was defined as:

$$\Delta\emptyset_{ij}(t)=\emptyset_i(t)-\emptyset_j(t) \quad (7)$$

The dPLI characterizes directed connectivity by quantifying the proportion of time points within a given time window at which the phase of one channel leads or lags that of another channel. It is calculated as follows:

$$dPLI_{ij}=\frac{1}{N}\sum_{t=1}^{N} H(sin(\Delta\emptyset_{ij}(t))) \quad (8)$$

where N is the total number of samples in the time series, and H(x) is the unit step function, with H(x)=1 when x>0 and H(x)=0 otherwise.The dPLI ranges from 0 to 1.A $dPLI_{ij}$ value greater than 0.5 indicates that the phase of node i generally leads that of node j, whereas a value below 0.5 indicates that the phase of node i generally lags that of node j. A value close to 0.5 indicates the absence of a stable phase-leading or phase-lagging relationship between the two nodes (Stam & van Straaten, 2012).

To characterize the topological roles of nodes in the directed functional connectivity network, the out-degree(D_{out})and in-degree(D_{in})of each node were calculated. D_{out} was defined as the number of suprathreshold directed edges from a given node to other nodes, whereas D_{in} was defined as the number of suprathreshold directed edges from other nodes to that node. Based on the relationship between these two measures, the nodes were categorized into three types:

(1)When $D_{out}> D_{in}$, the node was classified as a source node, indicating a greater number of outgoing connections.

(2)When $D_{in} > D_{out}$, the node was classified as a sink node, indicating a greater number of incoming connections.

(3)When $D_{out} \approx D_{in}$, the node was classified as a balanced node, indicating comparable numbers of incoming and outgoing connections.

The total degree, $D_{total}=D_{out}+D_{in}$ was used to characterize the overall connectivity of each node and was mapped to node size in the brain network visualizations. All graph-theoretical analyses were implemented using the MATLAB Brain Connectivity Toolbox (BCT; version 2019-03-03).

1.5 Classification and Decoding

1.5.1 Within-Subject Grip-Force-Level Decoding Using EEGSym

In recent years, hybrid convolution–Transformer architectures have been applied to spatiotemporal feature decoding and visualization of MI-EEG signals (Song et al., 2023). To evaluate model generalization across MI trials within the same participant and compare the classification difficulty among the three grip-force-level tasks, EEGSym (Pérez-Velasco et al., 2022) was employed for within-subject decoding. The data from each participant were independently used for model training and testing.

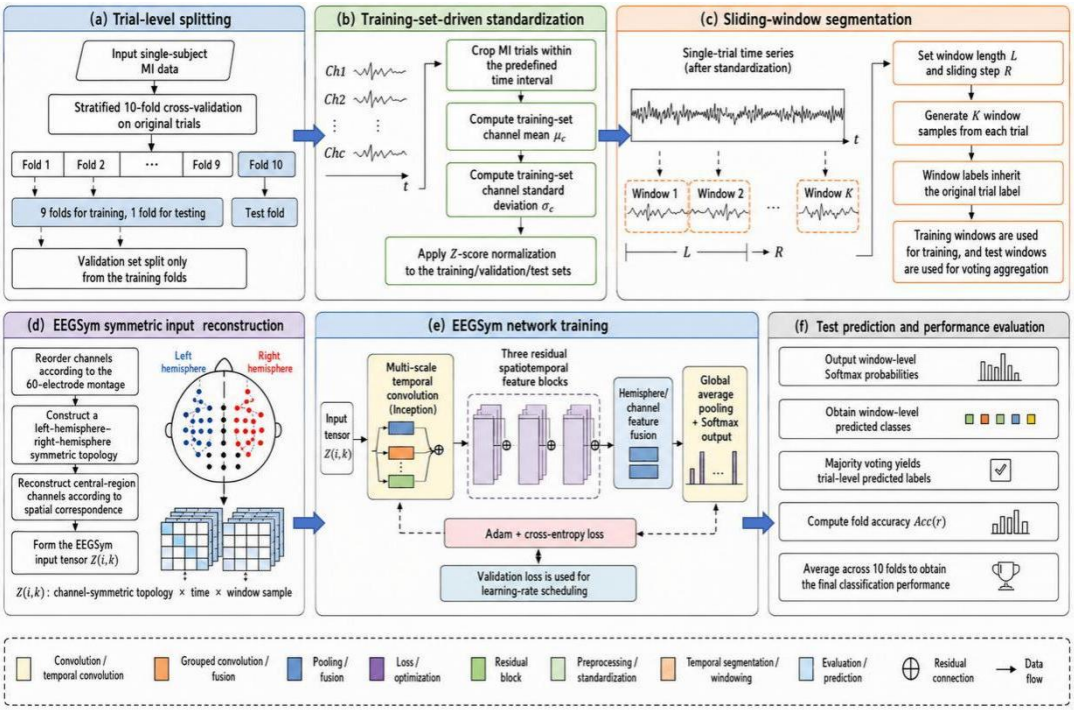


Fig. 2. EEGSym-based grip-force-level motor imagery decoding pipeline

Let the MI dataset of participant s be defined as:

$$D^{(s)}=\left\{\left(X_i^{(s)},y_i^{(s)}\right)\right\}_{i=1}^{N_s},\ X_i^{(s)}\in R^{C\times T},\ y_i^{(s)}\in\{0,1,2\} \tag{9}$$

where $X_i^{(s)}$ denotes the multichannel EEG signal of the i-th MI trial from participant s; C and T denote the number of channels and time samples, respectively; $y_i^{(s)}$ is the corresponding class label; N_s is the number of MI trials available for participant s. In the three-class task, labels 0, 1, and 2 represent the Low, Medium, and High grip-force motor imagery conditions, respectively.

In addition, three pairwise binary classification tasks were constructed: Low versus Medium, Low versus High, and Medium versus High. For each task, trials belonging to the corresponding two classes were selected, and their original labels were remapped to binary labels as follows:

$$y_i' = \begin{cases} 0, y_i = a \\ 1, y_i = b \end{cases} \qquad (a,b) \in \{(0,1),(0,2),(1,2)\} \tag{10}$$

The model input comprised the interval from 0.5 to 6.0 s after MI cue onset, sampled at 200 Hz. To prevent data leakage caused by the sliding-window procedure, data partitioning was performed at the original-trial level. For each participant, 90% of the trials were assigned to the training set and the remaining 10% to an independent test set. Stratified 10-fold cross-validation was conducted exclusively within the training set. The independent test set was not used for estimating normalization parameters, model training, hyperparameter tuning, or model selection.

The EEG signals were standardized using Z-scores. For each cross-validation model, the mean and standard deviation were estimated only from the corresponding training fold and then applied to the validation fold and independent test set. The standardized signal was calculated as

$$\widetilde{X}_{i,c,t} = \frac{X_{i,c,t} - \mu_c}{\sigma_c + \varepsilon} \tag{11}$$

where μ_c and σ_c denote the mean and standard deviation, respectively, of channel c estimated from the current training fold, and ε is a small constant introduced to prevent division by zero.

Each cropped trial was segmented using a sliding window with a length of 2.0 s, corresponding to L=400 samples, and a step size of 0.25 s, corresponding to R=50 samples. The number of windows generated from a single trial was calculated as

$$K = \left\lfloor \frac{T' - L}{R} \right\rfloor + 1 \tag{12}$$

where T' denotes the number of samples in the cropped trial. The k-th window of the i-th trial was expressed as:

$$W_{i,k}=\widetilde{X}_i[:,(k\text{-}1)R+1:(k\text{-}1)R+L], \quad k=1,2,\ldots,K \tag{13}$$

Based on the spatial locations of the 60 electrodes, EEGSym reorganized the channels into left-hemispheric, right-hemispheric, and central groups. Each hemisphere contained 26 lateral electrodes, while the eight central electrodes were duplicated and incorporated into both hemispheric representations, resulting in 34 channel positions for each side. Accordingly, the input tensor for each window had dimensions of 400×34×2×1, where the third dimension represented the left- and right-hemispheric structures.

The network comprised multiscale temporal convolution, residual spatiotemporal feature extraction, bilateral hemispheric fusion, temporal feature fusion, and Softmax classification modules. The multiscale temporal convolution module consisted of three parallel three-dimensional convolutional branches with kernel lengths of 500, 250, and 125 ms, corresponding to 100, 50, and 25 samples, respectively. Each branch contained 24 filters. The features extracted by the three branches were concatenated and added to a 1×1×1 residual projection, followed sequentially by batch normalization, exponential linear unit (ELU) activation, average pooling, and dropout.

The network then stacked three residual spatiotemporal feature blocks, in which 3×1×1 and 1×3×1 three-dimensional convolutions were used to extract temporal and spatial features, respectively. Subsequently, a 1×34×2 three-dimensional convolution jointly fused the channel information and bilateral hemispheric features. Temporal information was further integrated using a 3×1×1 convolution followed by global average pooling. The output module consisted of four 1×1×1 convolutional layers, each containing 32 filters, followed by a flattening layer and a fully connected Softmax layer. The numbers of output nodes were 2 and 3 for the binary and three-class tasks, respectively.

The model was trained using the Adam optimizer and the cross-entropy loss function. The initial learning rate was 1×10^{-3}, the batch size

was 22, the maximum number of training epochs was 20, and the dropout rate was 0.25. The convolutional kernels were initialized using the He normal initialization scheme. When the validation loss did not decrease for eight consecutive epochs, the learning rate was reduced to 0.5 times its current value, with a minimum learning rate of 1×10^{-6}.The random seed was set to 42.

During testing, the 10 cross-validation models independently generated Softmax probabilities for each window in the independent test set. Let $P_{i,k,c}^{(r)}$ denote the probability assigned to class c by the r-th model for the k-th window of the i-th test trial. The ensemble probability was calculated as

$$\overline{P}_{i,k}=\frac{1}{10}\sum_{r=1}^{10}P_{i,k,c}^{(r)} \tag{14}$$

The window-level predicted class was defined as

$$\hat{y}_{i,k}=arg\max_{c\in C}\overline{p}_{i,k,c} \tag{15}$$

Where C denotes the set of classes. Each test trial contained 15 windows, and the final trial-level label was determined by majority voting across the window-level predictions. The number of windows in the i-th trial predicted as class c was calculated as

$$n_{i,c}=\sum_{k=1}^{K}\mathrm{I}\left(\hat{y}_{i,k}=c\right) \tag{16}$$

The trial-level predicted label was defined as

$$\hat{y}_i=arg\max_{c\in C}n_{i,c} \tag{17}$$

When two or more classes received the same maximum number of votes, the class with the highest mean Softmax probability was selected. The trial-level classification accuracy on the test set was calculated as

$$\mathrm{Acc}=\frac{1}{N_{test}}\sum_{i=1}^{N_{test}}\mathbb{I}\left(\hat{y}_i=y_i\right) \tag{18}$$

Here,N_{test} denotes the number of original MI trials in the independent test set;$\hat{y}_i$ and y_i denote the predicted and true labels, respectively, of the i-th test trial;and $\mathbb{I}(\cdot)$is the indicator function,which equals 1 when $\hat{y}_i=y_i$ and 0 otherwise.

1.5.2 Conventional Machine-Learning Baselines

To obtain reference performance for conventional machine-learning methods, an MDM–SVM dual-branch probability-weighted fusion model based on FBCSP spatial filtering was constructed, with the individual MDM and SVM models included as comparison baselines. The procedure comprised adaptive time-window optimization, FBCSP feature extraction (Ang et al., 2012; Siviero et al., 2023), training of the two classifiers, and adaptive weighted fusion, as illustrated in Fig. 3.

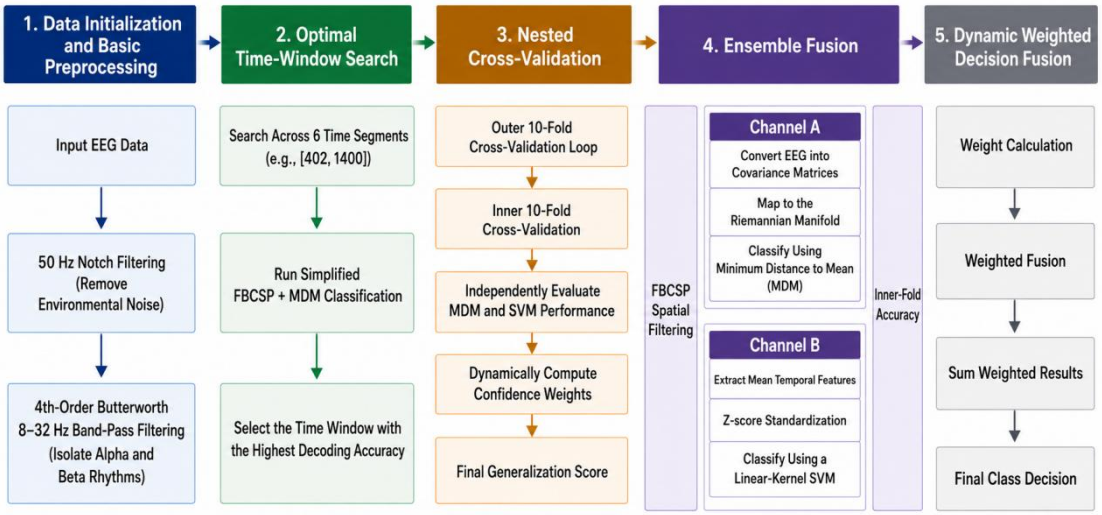


Fig. 3. Decoding pipeline of the MDM–SVM probability-weighted fusion model based on dual-stream features

First, time-window selection was performed within the outer training set. The candidate windows were −2 to 7 s,−1 to 6 s,0 to 5 s,1 to 4 s,−1 to 5 s,and 0 to 6 s.For each candidate window, the EEG signals were first subjected to 50 Hz notch filtering and 8-32 Hz band-pass filtering. Classification performance was then evaluated using internal cross-validation within the training set, and the window yielding the highest validation accuracy was selected for the current outer fold. The outer test set was not involved in time-window selection, feature standardization, spatial-filter estimation, classifier training, or fusion-weight calculation.

After the optimal time window had been determined, two classification branches based on MDM and SVM were constructed. In the SVM branch, the EEG signals were divided into three sub-bands: 8-14 Hz, 14-20 Hz, and 20-26 Hz. CSP spatial filtering was then performed

separately within each sub-band. For each sub-band, two CSP spatial-filter components corresponding to the largest generalized eigenvalues and two corresponding to the smallest generalized eigenvalues were retained, resulting in four spatial-filter components. The CSP features from all sub-bands were subsequently concatenated to form the FBCSP feature vector, which was classified using an SVM with a linear kernel.

The MDM branch performed Riemannian-geometric classification based on the channel covariance matrix of each trial. The Riemannian mean of the covariance matrices was first calculated for each class using the training samples. The geodesic distance between the covariance matrix of each test sample and the Riemannian mean of each class was then computed to obtain the corresponding class scores. Thus, the SVM branch primarily characterized the discriminative information of the FBCSP features in Euclidean space, whereas the MDM branch exploited the geometric structure of covariance matrices on the Riemannian manifold.

The fusion weights of the two branches were determined according to their cross-validation accuracies within the outer training set. Let Acc_{MDM} and Acc_{SVM} denote the validation accuracies of the MDM and SVM branches, respectively. The normalized weights were defined as

$$\mathrm{W_{MDM}}=\frac{\mathrm{Acc_{MDM}}}{\mathrm{Acc_{MDM}}+\mathrm{Acc_{SVM}}},\mathrm{W_{SVM}}=\frac{\mathrm{Acc_{SVM}}}{\mathrm{Acc_{MDM}}+\mathrm{Acc_{SVM}}} \tag{19}$$

Where $\mathrm{W_{MDM}}+\mathrm{W_{SVM}}=1$. During outer-fold testing, the class-specific outputs of the MDM and SVM branches were converted into normalized probabilities, denoted by P_{MDM} and P_{SVM}, respectively. For class c of test sample x, the fused probability was calculated as

$$P_{fusion}(c|x)=\mathrm{W_{MDM}P_{MDM}}+\mathrm{W_{SVM}P_{SVM}} \tag{20}$$

The final predicted class was defined as

$$\hat{y}=arg\max_{c} P_{fusion}(c|x) \tag{21}$$

The class with the highest fused probability was assigned as the predicted class. Time-window selection, CSP filter estimation, feature standardization, classifier training, and fusion-weight calculation were all restricted to the outer training set, whereas the outer test set was used only for final evaluation.

1.6 Statistical Analysis

For the analyses of MRCP features and classification performance, each participant was treated as the statistical unit. For the group-level analysis of brain network topology, electrode nodes were treated as repeated-measures units. The significance level was set at $p<0.05$.

For the MRCP analysis, the Early RP mean amplitude, NS mean amplitude, MP peak amplitude, and MP latency were extracted from channels C3, Cz, and C4. For each channel and each measure, a one-way repeated-measures analysis of variance was performed, with grip-force condition (Low, Medium, and High) as the within-participant factor. When a significant main effect of condition was identified, post hoc pairwise comparisons were conducted with Holm correction. A two-way repeated-measures analysis of variance with channel (C3, Cz, and C4) and condition (Low, Medium, and High) as within-participant factors was also performed to examine the interaction effect.

Sensorimotor rhythm activity was examined based on the ERSP results, with particular attention to ERD/ERS changes in the Alpha (8-13 Hz) and Beta (13-30 Hz) bands. Time–frequency maps and scalp topographies at C3, Cz, and C4 were used to characterize the duration, frequency distribution, and spatial distribution of ERD/ERS under the different grip-force conditions.

For the functional brain network analysis, directed functional connectivity networks were constructed using dPLI, and the out-degree, in-degree, and total degree of each node were calculated in the Delta, Theta, Alpha, Beta, and Gamma bands. At the node level, electrode nodes were treated as repeated-measures units. The Friedman test was used to assess overall differences in network measures among the three grip-force conditions. When a significant overall difference was detected, pairwise comparisons were performed using the Wilcoxon signed-rank test, with false discovery rate (FDR) correction applied to account for multiple comparisons. Kendall's W was reported as the effect-size measure.

Classification performance was expressed as the mean accuracy±standard deviation. A one-sample Wilcoxon signed-rank test was used to compare classification accuracy with the corresponding theoretical

chance level. Friedman tests were used to compare the accuracies of different models within the same classification task and the accuracies of the same model across different classification tasks. When a significant overall difference was found, post hoc pairwise comparisons were performed using paired t-tests with Holm correction.

2. Results

2.1 Movement-Related Cortical Potential Analysis

Figure 4 presents the mean MRCP waveforms recorded at C3, Cz, and C4 under the Low, Medium, and High grip-force conditions. Movement-related slow potential changes were observed around MI cue onset under all three conditions, with a negative deflection emerging after cue presentation. Compared with C3 and Cz, C4 exhibited more pronounced waveform differences among the three grip-force conditions, particularly during the time intervals corresponding to the Early RP, NS, and MP components.

Statistical analysis revealed significant main effects of grip-force condition on the Early RP mean amplitude, NS mean amplitude, and MP peak amplitude at C4. Under the Low, Medium, and High conditions, the Early RP mean amplitudes at C4 were −0.070±0.062μV,−0.007±0.096μV and −0.027±0.092μV,respectively, with a significant main effect of grip-force condition[$F(2,22)=5.39$, $p=0.013$].The corresponding NS mean amplitudes were 0.175±0.228μV,−0.042±0.301μV and −0.007±0.227μV, respectively, also showing a significant main effect of grip-force condition [$F(2,22)=3.57$, $p=0.046$].

The MP peak amplitudes at C4 were −1.772±0.826μV,−2.233±0.769μV and −2.077±1.199μV, under the Low, Medium, and High conditions, respectively. A significant difference was observed among the three grip-force conditions [$F(2,22)=4.07$, $p=0.031$]. Holm-corrected pairwise comparisons showed that the MP peak amplitude under the Medium condition was significantly lower than that under the Low condition ($p=0.027$). No significant difference in MP latency at C4 was detected among the three grip-force conditions($p>0.05$).

No significant main effects of grip-force condition were detected for the Early RP mean amplitude, NS mean amplitude, MP peak amplitude, or MP latency at C3 or Cz ($p>0.05$). The two-way repeated-measures analysis of variance with channel (C3, Cz, and C4) and condition (Low, Medium, and High) as within-participant factors revealed significant channel-by-condition interactions for the Early RP and NS mean amplitudes, with $p=0.042$ and $p=0.041$, respectively. These findings indicate that the effects of grip-force condition on the Early RP and NS varied across electrode locations. The interaction effects for MP peak amplitude and MP latency did not reach statistical significance.

Overall, MRCP differences associated with grip-force-level motor imagery were primarily observed at C4, where the Early RP mean amplitude, NS mean amplitude, and MP peak amplitude were significantly modulated by grip-force condition. However, none of the MRCP measures exhibited a consistent monotonic increase or decrease from the Low to Medium and High conditions.

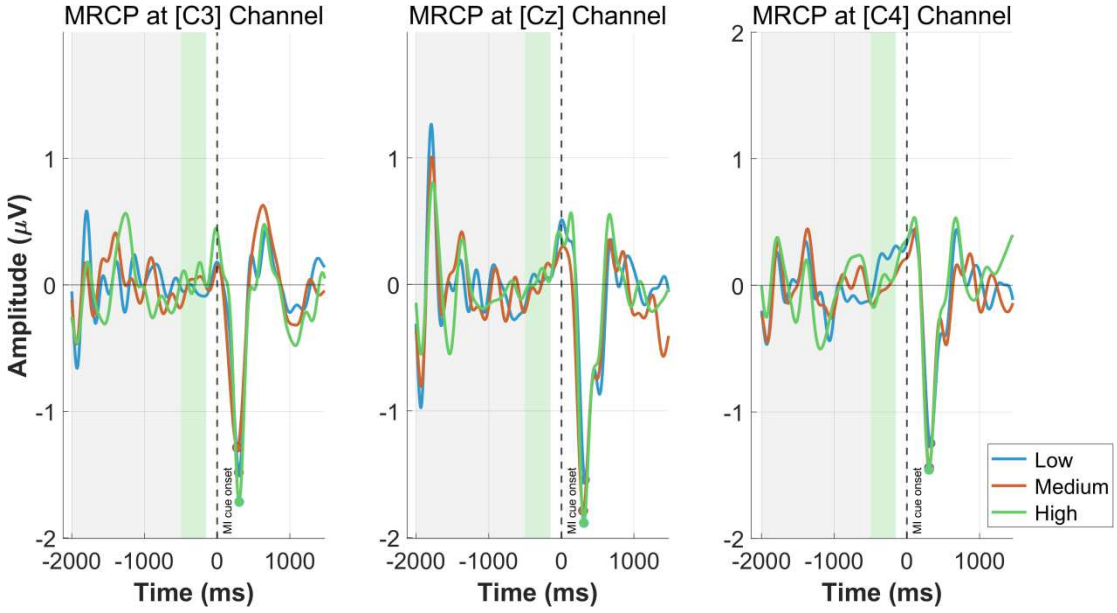


Fig. 4. Mean MRCP waveforms under different grip-force conditions

2.2 Time–Frequency and Spatial Characteristics of Sensorimotor Rhythms

Figure 5 presents the ERSP time–frequency distributions at C3, Cz, and C4 under the Low, Medium, and High grip-force conditions, together

with scalp topographies for the Alpha (8-13 Hz) and Beta (13-30 Hz) bands. The MI cue onset was defined as 0 s. The time–frequency maps display spectral power changes from approximately 1 s before to 6 s after cue onset, whereas the scalp topographies illustrate the spatial power distributions of the Alpha and Beta bands during the core MI period. Negative ERSP values indicate a reduction in power relative to baseline, corresponding to ERD.

Alpha- and Beta-band ERD emerged after MI onset under all three grip-force conditions, indicating that grip-force-level motor imagery elicited suppression of sensorimotor rhythms. Compared with Cz, the Alpha- and Beta-band power reductions were more clearly observed at C3 and C4. Under the Low condition, Alpha/Beta ERD was relatively brief and spatially restricted. Under the Medium condition, the ERD distribution became more extensive. Under the High condition, sustained power reductions were observed at C3, Cz, and C4, with particularly pronounced suppression in the Beta band. The scalp topographies showed that Alpha-band power changes were broadly distributed across the central sensorimotor and parieto-occipital regions, whereas Beta-band changes were primarily concentrated over the central region and its surrounding areas. Compared with the Low and Medium conditions, the High condition exhibited more pronounced Beta-band power suppression over the central region and a broader spatial distribution of Alpha-band activity.

Overall, Alpha/Beta ERD was observed under all three grip-force conditions. As the grip-force level increased, ERD tended to become more sustained and to extend across a broader frequency and spatial range, with the most evident effect being enhanced Beta-band suppression over the central region under the High condition.

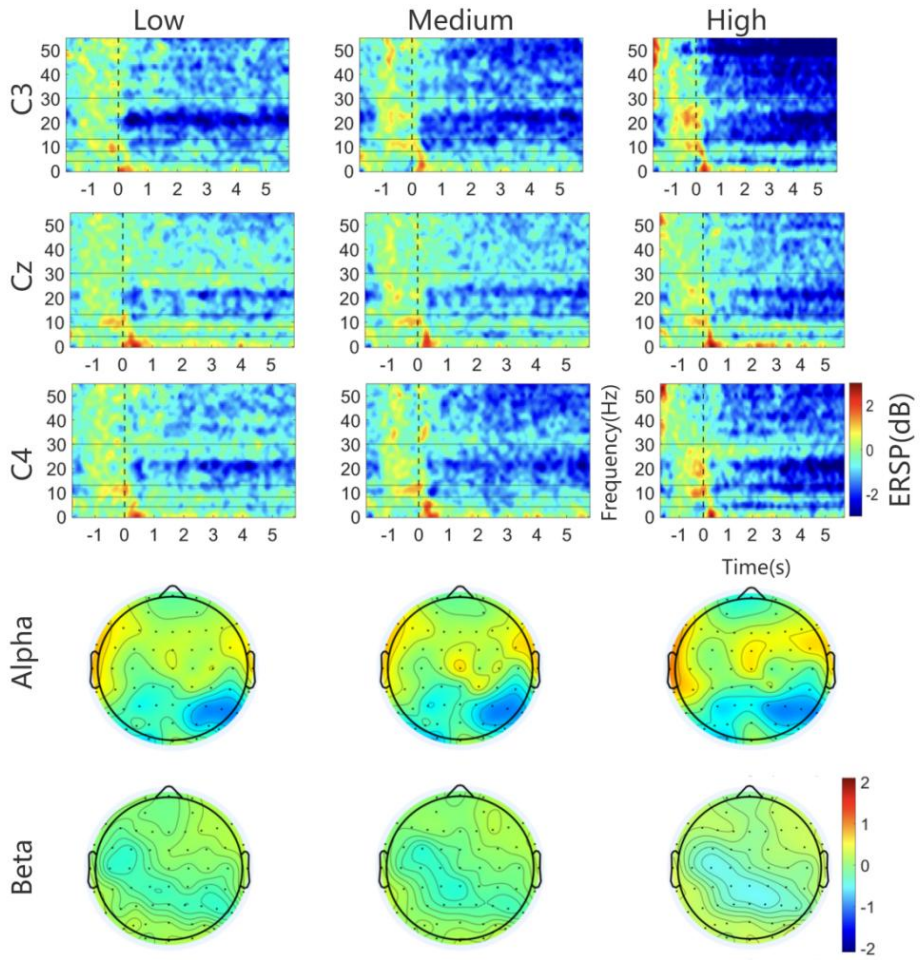


Fig. 5. Spatiotemporal dynamics of sensorimotor EEG rhythms under different force-load conditions

2.3 Topological Analysis of Directed Functional Brain Networks

To obtain group-level directed functional connectivity patterns, the dPLI matrices of all participants were averaged within each grip-force condition and frequency band to construct group-level weighted directed connectivity matrices. Because threshold selection affects global network efficiency and topological stability, network metrics were compared across thresholds ranging from 0.55 to 0.80. As shown in Fig. 6, global efficiency initially increased and subsequently decreased as the threshold increased, whereas topological stability remained relatively high within the intermediate threshold range. At a threshold of 0.65, the network retained both relatively high global efficiency and topological stability. Therefore,

0.65 was selected as the binarization threshold for the subsequent analyses.

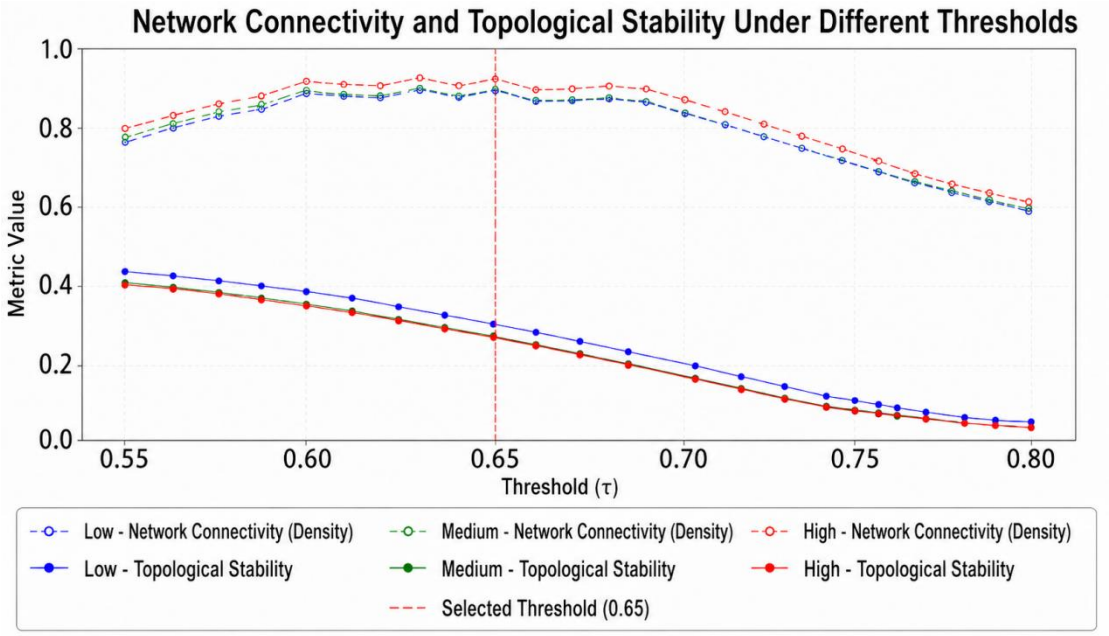


Fig. 6. Changes in brain network connectivity and topological stability across different dPLI thresholds

Figure 7 presents the group-level directed functional connectivity networks in the Alpha and Beta bands under the Low, Medium, and High grip-force conditions, whereas Fig. 8 shows the differences in node in-degree and out-degree between conditions. Differences were calculated as "A–B"; positive values indicate a higher node degree under condition A, whereas negative values indicate a lower degree. Directed connections were observed under all three grip-force conditions and primarily involved nodes in the central, centroparietal, frontocentral, and occipital regions. In the Alpha and Beta bands, C3, C4, and CP1-CP4 predominantly acted as source nodes($D_{out}>D_{in}$), whereas F3, FC1, FC2, O1, and O2 acted as sink nodes($D_{in}>D_{out}$)under some conditions. Cz exhibited relatively balanced in-degree and out-degree.

The between-condition differences showed that changes in node degree were frequency- and region-specific. Differences in the Delta and Theta bands were primarily distributed over C3, C4, several CP electrodes, F3, and occipital nodes. Differences in the Alpha and Beta bands mainly involved the central sensorimotor, centroparietal, and selected frontocentral nodes, whereas Gamma-band differences were more spatially

dispersed. Local changes in node degree were observed in all three pairwise comparisons; however, the direction of change varied across frequency bands and nodes, without a consistent monotonic pattern. The High–Low comparison involved a greater number of central and parietal nodes, indicating more extensive directed network differences between the nonadjacent grip-force levels.

To assess the overall differences in node-degree distributions among the grip-force conditions, electrode nodes were treated as repeated-measures units. The out-degree(D_{out}), in-degree(D_{in})and total degree(D_{total})were compared among the Low, Medium, and High conditions within each frequency band. Friedman tests were used to evaluate the overall condition effects. The resulting p-values for D_{out},D_{in} and D_{total} across the five frequency bands were adjusted using the Benjamini–Hochberg false discovery rate procedure and are reported as p_{FDR}. When the overall test was significant, pairwise comparisons were performed using Wilcoxon signed-rank tests, with FDR correction applied across the three pairwise comparisons within the corresponding frequency band and network measure.

The Friedman test showed significant condition effects on node out-degree in the Delta band [$x^2(2)$=17.074, p_{FDR}=0.00098, W=0.164], Alpha band [$x^2(2)$ =7.743, p_{FDR} =0.0386,W=0.074],and Gamma band [$x^2(2)$ =7.529, p_{FDR} =0.0386,W=0.072].Significant condition effects on node in-degree were also observed in the Delta band [$x^2(2)$ =21.540, p_{FDR} =0.000105,W=0.207],Alpha band [$x^2(2)$ =10.941, p_{FDR} =0.0105,W=0.105], and Gamma band [$x^2(2)$ =8.818, p_{FDR} =0.0203,W=0.085]. The condition effects on total degree were more pronounced and reached significance in the Delta band [$x^2(2)$ =34.288, p_{FDR} <0.001,W=0.330], Alpha band [$x^2(2)$ =17.673, p_{FDR} =0.00036,W=0.170], and Gamma band [$x^2(2)$=14.870,p_{FDR}=0.00098,W=0.143]. In terms of effect size, the largest condition effect was observed in the Delta band, whereas the effects in the Alpha and Gamma bands were relatively smaller.

FDR-corrected pairwise comparisons showed that, in the Delta band, the Low condition exhibited a higher out-degree than the Medium

condition, while its in-degree and total degree were both higher than those under the Medium and High conditions. In the Alpha band, the Low condition showed a higher in-degree than the Medium condition and a higher total degree than both the Medium and High conditions. A different pattern was observed in the Gamma band: the High condition exhibited a higher in-degree than the Low condition and a higher total degree than both the Low and Medium conditions. These results indicate that the Low grip-force condition was primarily characterized by greater group-level node degrees in the Delta and Alpha bands, whereas the High grip-force condition was characterized by increased node degrees in the Gamma band.

Taken together, the threshold analysis, group-level network topology, node-difference maps, and nonparametric statistical results demonstrated cross-frequency and cross-regional topological differences in the dPLI-directed networks among grip-force conditions. Node degree was particularly sensitive to changes in grip-force level in the Delta, Alpha, and Gamma bands. Network connectivity was greater in the Delta and Alpha bands under the Low condition, whereas Gamma-band node degree increased under the High condition. These findings indicate that grip-force-level motor imagery changes both local sensorimotor rhythms and directed functional connectivity across brain regions.

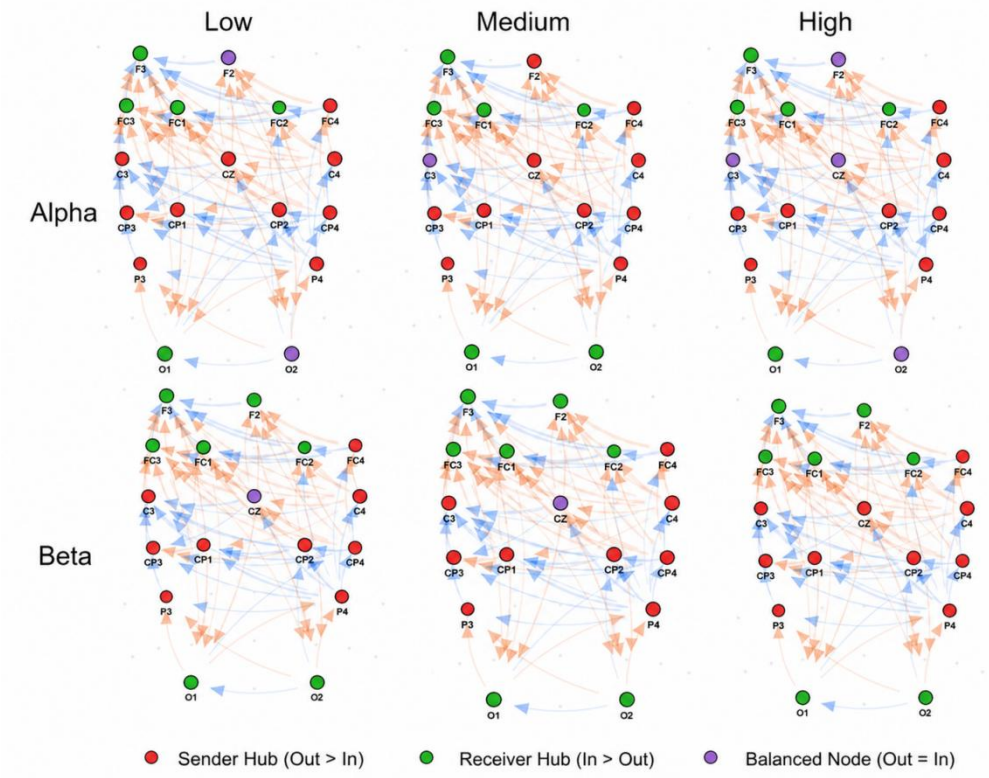


Fig. 7. Topology of dPLI-based directed brain networks in the Alpha and Beta bands

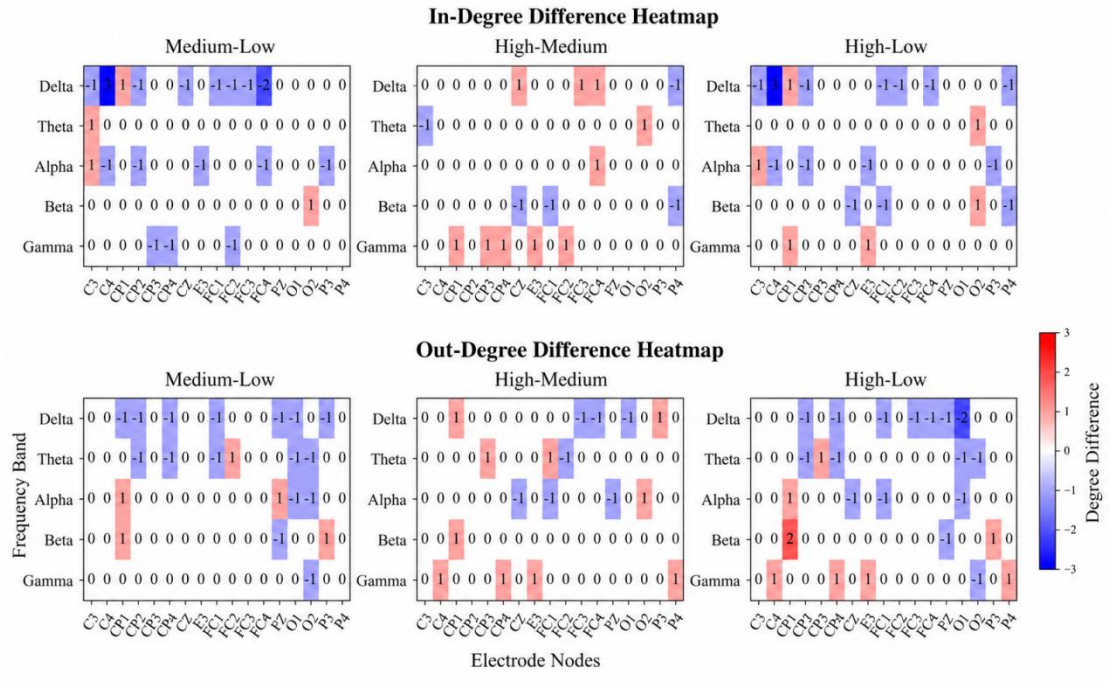


Fig. 8. Heatmaps of degree differences at key nodes between grip-force conditions

2.4 Decoding Performance of Grip-Force-Level Motor Imagery

Figure 9 and Table 1 summarize the classification accuracies of the four decoding models for the three pairwise binary classification tasks—Low versus Medium, Low versus High, and Medium versus High—and the three-class task involving Low, Medium, and High conditions.

EEGSym achieved the highest mean accuracy in all four tasks, with accuracies of 63.35%±16.01%, 77.81%±18.90%, 72.60%±15.23% and 62.01%±21.82%, respectively. The corresponding accuracies of the MDM–SVM fusion model were 61.52%±2.52%,71.24%±9.12%,65.98% ±8.60% and 44.65%±5.08%, respectively, and were consistently higher than those of the individual MDM and SVM models.

Using 50% for the binary tasks and 33.33% for the three-class task as the theoretical chance levels, one-sided exact Wilcoxon signed-rank tests were performed to determine whether the participant-level accuracies of

each model were significantly above chance. The MDM–SVM fusion model achieved accuracies significantly above the corresponding chance levels in all four tasks (all p_{adj}=0.004).EEGSym performed significantly above chance in the Low versus High task (p_{adj}=0.012), the Medium versus High task, and the three-class task (both p_{adj}=0.004), but not in the Low versus Medium task (p_{adj}=0.081). The individual MDM model performed significantly above chance only in the Low versus High task (p_{adj}=0.015), whereas the individual SVM model exceeded chance only in the three-class task (p_{adj}=0.015).

Holm-corrected pairwise comparisons between models showed that, in the Low versus Medium task, the MDM-SVM fusion model significantly outperformed MDM(p_{Holm}<0.001) and SVM(p_{Holm}=0.007). In the Low versus High task, the MDM-SVM fusion model significantly outperformed SVM(p_{Holm} <0.001), and EEGSym also significantly outperformed SVM(p_{Holm}=0.002);the difference between the MDM-SVM fusion model and MDM did not reach statistical significance (p_{Holm}=0.051). In the Medium versus High task, the MDM-SVM fusion model significantly outperformed both MDM and SVM (bothp_{Holm}=0.006),while EEGSym significantly outperformed MDM (p_{Holm} =0.015) and SVM(p_{Holm} =0.006).In the three-class task, EEGSym significantly outperformed the MDM – SVM fusion model (p_{Holm}=0.032),MDM(p_{Holm}=0.020) and SVM(p_{Holm}=0.009);the MDM-SVM fusion model also significantly outperformed MDM (p_{Holm}=0.020) and SVM(p_{Holm}=0.005).

Overall, EEGSym achieved the highest mean accuracy in all classification tasks and significantly outperformed the other models in the three-class task. Compared with the individual MDM and SVM models, the MDM–SVM fusion model produced more consistent performance improvements, indicating that probability-level fusion of SVM and MDM outputs enhanced classification based on FBCSP features. In terms of task difficulty, the Low versus High task yielded the highest overall accuracies, whereas the three-class task produced relatively lower accuracies. These findings indicate that nonadjacent grip-force levels were more readily

distinguishable than adjacent grip-force levels and that the simultaneous decoding of three grip-force levels remained more challenging.

Table 1

Classification accuracies of the four decoding models across different grip-force-level motor imagery tasks

Model	Low vs Medium	Low vs High	Medium vs High	Low vs Medium vs High
MDM-SVM	61.52±2.52	71.24±9.12	65.98±8.60	44.65±5.08
MDM	50.27±5.76	62.86±13.03	55.51±13.35	38.68±8.59
SVM	50.65±5.52	51.65±3.64	52.69±3.21	37.20±3.47
EEGSym	63.35±16.01	77.81±18.90	72.60±15.23	62.01±21.82

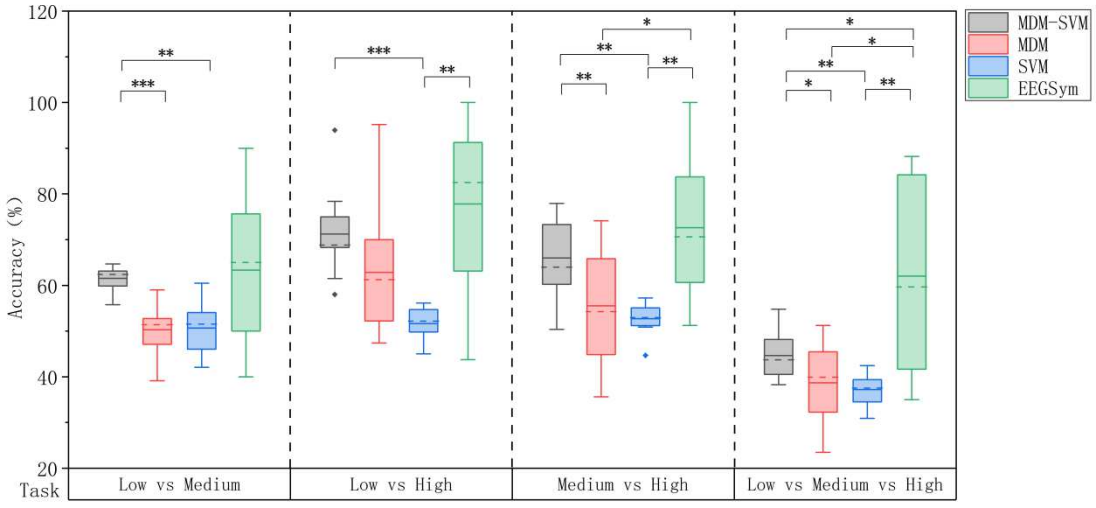


Fig. 9. Distribution of participant-level accuracies for the four decoding models across different classification tasks.Note: Overall differences among models were assessed using the Friedman test, followed by Holm-corrected paired t-tests for post hoc comparisons.∗p<0.05,

∗∗p<0.01

3. Discussion

Compared with previous studies that focused mainly on a single EEG feature or classification performance, this study established three grip-force conditions 10%, 50%, and 90% MVC within a unified experimental paradigm and used MRCP, ERSP, and dPLI to characterize grip-force-level

motor imagery from three perspectives: movement-preparation-related slow potentials, sensorimotor rhythms, and directed functional connectivity. Differences among grip-force conditions were not confined to a single time interval, frequency band, or brain region; instead, they appeared in slow-potential modulation, local rhythmic suppression, and cross-regional network reorganization. These findings indicate that no single feature fully captures the neural representation of grip-force-level motor imagery and that multidimensional analyses provide complementary information.

Within the same data-partitioning and evaluation framework, three pairwise binary classification tasks and one three-class task were used to compare EEGSym, the MDM–SVM fusion model, and its individual branches. The results confirmed that the three grip-force intentions could be decoded and showed that nonadjacent grip-force levels were easier to distinguish than adjacent levels, whereas simultaneous discrimination among all three grip-force levels was more challenging. Accordingly, this study combines a three-level grip-force paradigm, multidimensional neurophysiological analysis, and classification decoding within a unified framework. By examining grip-force-level motor imagery from both neural representation and decoding-performance perspectives, this study provides experimental evidence that fine-grained grip-force intentions can be decoded for graded rehabilitation control.

3.1 Cortical Responses and Network Reorganization across Grip-Force Levels

As shown in Fig. 4, MRCP waveform changes were observed at C3, Cz, and C4 under all three grip-force conditions, with more pronounced between-condition differences at C4. Statistical analysis revealed significant main effects of grip-force condition on the Early RP mean amplitude, NS mean amplitude, and MP peak amplitude at C4, although none of these measures changed monotonically as grip-force level increased. These findings indicate that MRCPs reflect motor preparation and task initiation during grip-force-level motor imagery, but do not reliably distinguish adjacent grip-force levels. The Early RP, NS, and MP

correspond to the classical phases of the readiness potential, and their variations reflect slow-potential changes during the formation of motor intention and preparation for motor imagery.

As shown in Fig. 5, all three grip-force conditions elicited Alpha- and Beta-band ERD, manifested as power reductions within 8–30 Hz at C3, Cz, and C4 after MI onset. Under the High condition, ERD was more sustained and spatially extensive, with particularly strong Beta-band power suppression over the central region. The scalp topographies showed that Beta-band changes were primarily concentrated over the central sensorimotor cortex, whereas Alpha-band changes were more broadly distributed and extended toward parieto-occipital regions. These results indicate that grip-force-level motor imagery involves not only modulation of central sensorimotor rhythms but also the participation of more widely distributed cortical regions.

As shown in Figs. 7 and 8, differences in dPLI-based directed networks were not restricted to a single node or frequency band but were distributed across central sensorimotor, centroparietal, frontocentral, and occipital nodes. Directed connectivity was observed in both the Alpha and Beta bands. Several central and centroparietal nodes acted as source nodes, whereas some frontocentral and occipital nodes acted as sink or balanced nodes. The between-condition difference maps further showed that changes in node in-degree and out-degree were frequency- and node-specific. Together with the statistical results, these findings indicate that node degree in the Delta, Alpha, and Gamma bands was particularly sensitive to changes in grip-force level. Thus, grip-force-level motor imagery altered not only local spectral activity but also the group-level topology of directed functional networks.

Taken together, MRCP, ERSP, and dPLI showed different sensitivities across grip-force levels. MRCP primarily reflected slow-potential changes related to movement preparation, ERSP revealed suppression of sensorimotor rhythms, and dPLI characterized directed connectivity across brain regions. No single feature fully described the neural representation of grip-force-level motor imagery; instead, the multilevel analyses provided complementary information. This interpretation is consistent with

previous findings that ERD/ERS, functional connectivity, and multimodal feature fusion can improve both the classification performance and interpretability of MI-BCI systems (Kim et al., 2018; Leeuwis et al., 2021; Mussi & Adams, 2022; Siviero et al., 2023; Zhang et al., 2016; Zhao et al., 2018).

3.2 Feasibility of Decoding Grip-Force-Level Motor Imagery

The classification results showed that EEG recorded during grip-force-level motor imagery contained discriminative information for decoding grip-force intentions. For EEGSym, the MDM–SVM fusion model, and MDM, the Low versus High task yielded the highest mean binary classification accuracy, whereas the three-class task generally produced lower accuracies than the binary tasks. These findings indicate that EEG patterns differed more clearly between nonadjacent grip-force levels. By contrast, adjacent grip-force levels, such as Low versus Medium and Medium versus High, were more difficult to distinguish, and simultaneous recognition of all three grip-force levels remained challenging.

EEGSym achieved the highest mean accuracy in all three binary tasks and the three-class task and significantly outperformed the MDM–SVM fusion model, MDM, and SVM in the three-class task, showing that it can effectively distinguish multiple grip-force intentions. EEGSym exploits the spatial correspondence between electrodes over the left and right hemispheres through hemispheric symmetric reconstruction and uses multiscale spatiotemporal convolutions to extract dynamic EEG features at different temporal scales, thereby improving its ability to distinguish subtle differences among grip-force levels (Altaheri et al., 2023; Liu et al., 2023; Pérez-Velasco et al., 2022).

The MDM–SVM fusion model achieved higher mean accuracy than the individual MDM and SVM models in all four tasks, indicating that the discriminative information captured by SVM from FBCSP features was complementary to the Riemannian-geometric representation used by MDM. Probability-weighted fusion therefore improved classification performance within the conventional machine-learning framework. The

difference between the MDM–SVM fusion model and MDM did not reach statistical significance only in the Low versus High binary task; in the remaining relevant model comparisons, the fusion model significantly outperformed the individual MDM or SVM model. Overall, EEGSym showed a more pronounced advantage in multiclass decoding, whereas the MDM–SVM fusion model produced relatively consistent performance gains in the binary tasks.

3.3 Limitations and Future Directions

This study has several limitations. First, the experiment was based on offline EEG data from only 12 healthy participants and did not include patients with stroke or other motor impairments. The applicability of the findings to clinical rehabilitation populations therefore requires further validation. Second, the evaluation was primarily conducted within participants, and the generalization performance of the models across participants, sessions, and long-term repeated measurements was not systematically examined. In addition, the spatial distributions of the MRCP, ERSP, and dPLI results exhibited a certain degree of regional specificity and hemispheric lateralization.

At the application level, future studies should extend the current offline analysis to online closed-loop validation. The Low, Medium, and High grip-force intentions could be mapped to graded control commands for rehabilitation robots, functional electrical stimulation systems, intelligent prostheses, or biomimetic robotic hands. Continuous contingent feedback, adaptive confidence thresholds, and safety-oriented control mechanisms should also be incorporated to evaluate the real-time performance, stability, safety, and practical utility of the proposed approach in fine motor rehabilitation and assistive control applications (Biasiucci et al., 2018).

4. Conclusion

This study investigated Low, Medium, and High grip-force conditions using an ME-guided MI paradigm. MRCP, ERSP, and dPLI analyses were

used to characterize EEG responses during grip-force-level motor imagery, and the decoding performance of EEGSym and FBCSP-based MDM/SVM models was compared.

The results showed multilevel differences in EEG responses across grip-force conditions. MRCP differences were mainly observed at C4, where the Early RP mean amplitude, NS mean amplitude, and MP peak amplitude showed significant effects of grip-force condition but did not change monotonically as grip-force level increased. The ERSP results showed that all three grip-force conditions elicited Alpha/Beta ERD, with more pronounced Beta-band power suppression over the central region under the High condition. The dPLI network analysis further revealed frequency- and region-dependent differences in node out-degree, in-degree, and total degree, with the Delta, Alpha, and Gamma bands showing greater sensitivity to changes in grip-force level.

The classification results showed that EEGSym achieved the highest mean accuracy in all three binary tasks and the three-class task, whereas the MDM–SVM fusion model generally outperformed the individual MDM and SVM models. Classification accuracy was higher for comparisons between nonadjacent grip-force levels, whereas performance was lower in the three-class task. These findings indicate that nonadjacent grip-force levels are easier to distinguish than adjacent levels and that simultaneous decoding of multiple grip-force levels remains challenging.

Overall, EEG can identify motor-imagery intentions associated with different grip-force levels. MRCP, ERSP, and dPLI provide complementary information about the underlying neural representations, while EEGSym and the MDM–SVM fusion model show that grip-force intentions can be decoded. This study supports the development of grip-force-level MI-BCI systems and graded rehabilitation feedback control; however, generalizability across participants and applicability in online closed-loop systems and clinical populations require further validation.

CRediT authorship contribution statement

Yan Bian: Conceptualization, Methodology, Supervision, Project administration, Funding acquisition, Resources, Writing – review &

editing.

Zhao Jialing: Conceptualization, Methodology, Software, Formal analysis, Investigation, Data curation, Visualization, Writing – original draft, Writing – review & editing.

Tian Linqing: Investigation, Writing – review & editing.

Yu Xinting: Investigation, Writing – review & editing.

Jian Dong:Writing – review & editing.

Conflict of Interest declaration

The authors declare that they have no affiliations with or involvement in any organization or entity with any financial interest in the subject matter or materials discussed in this manuscript.

Acknowledgements

This work was supported in part by Tianjin Metrology Science and Technology Projects [grant number 2025TJMT016].

Data availability

The raw EEG data supporting the findings of this study are publicly available in Zenodo at https://doi.org/10.5281/zenodo.21470456.

References

Altaheri, H., Muhammad, G., & Alsulaiman, M. (2023). Physics-informed attention temporal convolutional network for EEG-based motor imagery classification. *IEEE Transactions on Industrial Informatics, 19(2), 2249–2258.* https://doi.org/10.1109/TII.2022.3197419

Ang, K. K., Chin, Z. Y., Wang, C., Guan, C., & Zhang, H. (2012).Filter bank common spatial pattern algorithm on BCI Competition IV datasets 2a and 2b. *Frontiers in Neuroscience, 6, Article 39.* https://doi.org/10.3389/fnins.2012.00039

Barachant, A., Bonnet, S., Congedo, M., & Jutten, C. (2012). Multiclass brain–computer interface classification by Riemannian geometry. *IEEE Transactions*

on Biomedical Engineering, 59(4), 920–928. https://doi.org/10.1109/TBME.2011.2172210

Biasiucci, A., Leeb, R., Iturrate, I., Perdikis, S., Al-Khodairy, A., Corbet, T., Schnider, A., Schmidlin, T., Zhang, H., Bassolino, M., Viceic, D., Vuadens, P., Guggisberg, A. G., & Millán, J. d. R. (2018). Brain-actuated functional electrical stimulation elicits lasting arm motor recovery after stroke. *Nature Communications, 9, Article 2421.* https://doi.org/10.1038/s41467-018-04673-z

Chen, C., Zhao, J., Zhang, X., Lu, B., Yao, D., Lu, J., Zhang, Y., Xu, P., Ma, X., & Li, F. (2026). Fine-grained upper limb force control relies on distributed functional connectivity during motor planning: A scalp EEG study. *IEEE Transactions on Neural Systems and Rehabilitation Engineering, 34, 2428–2437.* https://doi.org/10.1109/TNSRE.2026.3691778

Delorme, A., & Makeig, S. (2004). EEGLAB: An open source toolbox for analysis of single-trial EEG dynamics including independent component analysis. *Journal of Neuroscience Methods, 134(1), 9–21.* https://doi.org/10.1016/j.jneumeth.2003.10.009

Fu, Y., Chen, J., & Xiong, X. (2018). Calculation and analysis of microstate related to variation in executed and imagined movement of force of hand clenching. *Computational Intelligence and Neuroscience, 2018, Article 9270685.* https://doi.org/10.1155/2018/9270685

Jochumsen, M., Rovsing, C., Rovsing, H., Niazi, I. K., Dremstrup, K., & Kamavuako, E. N. (2017). Classification of hand grasp kinetics and types using movement-related cortical potentials and EEG rhythms. Computational *Intelligence and Neuroscience, 2017, Article 7470864.* https://doi.org/10.1155/2017/7470864

Karakullukcu, N., Altındiş, F., & Yılmaz, B. (2024). Object weight perception in motor imagery using Fourier-based synchrosqueezing transform and regularized common spatial patterns. *IEEE Access, 12, 52978–52989*. https://doi.org/10.1109/ACCESS.2024.3386554

Kim, Y. K., Park, E., Lee, A., Im, C.-H., & Kim, Y.-H. (2018). Changes in network connectivity during motor imagery and execution. *PLOS ONE, 13(1), Article e0190715.* https://doi.org/10.1371/journal.pone.0190715

Leeuwis, N., Yoon, S., & Alimardani, M. (2021). Functional connectivity analysis in motor-imagery brain computer interfaces. *Frontiers in Human Neuroscience, 15, Article 732946.* https://doi.org/10.3389/fnhum.2021.732946

Li, H., Ye, X., Liu, Y., Xie, T., Tan, W., Shen, Y., Wang, Q., Xiong, C., Wang, Y., Lin, W., & Long, J. (2023). A novel noninvasive brain–computer interface by imagining isometric force levels. *Cognitive Neurodynamics, 17(4), 975–983.* https://doi.org/10.1007/s11571-022-09875-2

Li, R., Liu, Y. Q., Liu, W. P., Wu, R., Bai, D. Y., Yang, D., Zhang, J. F., & Zhao, J. (2024). Study on a brain computer interface based on decoding of precise hand movements. *Journal of Clinical Neurosurgery, 21(4), 384–388, 395.* https://doi.org/10.3969/j.issn.1672-7770.2024.04.005

Liu, K., Yang, M., Yu, Z., Wang, G., & Wu, W. (2023). FBMSNet: A filter-bank multi-scale convolutional neural network for EEG-based motor imagery decoding. *IEEE Transactions on Biomedical Engineering, 70(2), 436–445.* https://doi.org/10.1109/TBME.2022.3193277

Ma, Z.-Z., Wu, J.-J., Cao, Z., Hua, X.-Y., Zheng, M.-X., Xing, X.-X., Ma, J., & Xu, J.-G. (2024). Motor imagery-based brain–computer interface rehabilitation programs enhance upper extremity performance and cortical activation in stroke patients. *Journal of NeuroEngineering and Rehabilitation, 21, Article 91.* https://doi.org/10.1186/s12984-024-01387-w

Mussi, M. G., & Adams, K. D. (2022). EEG hybrid brain–computer interfaces: A scoping review applying an existing hybrid-BCI taxonomy and considerations for pediatric applications. *Frontiers in Human Neuroscience, 16, Article 1007136.* https://doi.org/10.3389/fnhum.2022.1007136

Pan, L., Wang, K., Huang, Y., Sun, X., Meng, J., Yi, W., Xu, M., Jung, T.-P., & Ming, D. (2025). Enhancing motor imagery EEG classification with a Riemannian geometry-based spatial filtering method. *Neural Networks, 188, Article 107511.* https://doi.org/10.1016/j.neunet.2025.107511

Pérez-Velasco, S., Santamaría-Vázquez, E., Martínez-Cagigal, V., Marcos-Martínez, D., & Hornero, R. (2022). EEGSym: Overcoming inter-subject variability in motor imagery-based BCIs with deep learning. *IEEE Transactions on Neural Systems and Rehabilitation Engineering, 30, 1766–1775.* https://doi.org/10.1109/TNSRE.2022.3186442

Pérez-Velasco, S., Marcos-Martínez, D., Santamaría-Vázquez, E., Martínez-Cagigal, V., & Hornero, R. (2025). Bridging motor execution and motor imagery BCI paradigms: An inter-task transfer learning approach. *Biomedical Signal*

Processing and Control, 107, Article 107834. https://doi.org/10.1016/j.bspc.2025.107834

Rong, F., Yang, B., & Guan, C. (2024). Decoding multi-class motor imagery from unilateral limbs using EEG signals. *IEEE Transactions on Neural Systems and Rehabilitation Engineering, 32, 3399–3409.* https://doi.org/10.1109/TNSRE.2024.3454088

Saibene, A., Caglioni, M., Corchs, S., & Gasparini, F. (2023). EEG-based BCIs on motor imagery paradigm using wearable technologies: A systematic review. *Sensors, 23(5), Article 2798.* https://doi.org/10.3390/s23052798

Sheng, J., Xu, J., Li, H., Liu, Z., Zhou, H., You, Y., Song, T., & Zuo, G. (2023). A multi-scale temporal convolutional network with attention mechanism for force level classification during motor imagery of unilateral upper-limb movements. *Entropy, 25(3), Article 464.* https://doi.org/10.3390/e25030464

Shibasaki, H., & Hallett, M. (2006). What is the Bereitschaftspotential? *Clinical Neurophysiology, 117(11), 2341–2356.* https://doi.org/10.1016/j.clinph.2006.04.025

Siviero, I., Menegaz, G., & Storti, S. F. (2023). Functional connectivity and feature fusion enhance multiclass motor-imagery brain–computer interface performance. *Sensors, 23(17), Article 7520.* https://doi.org/10.3390/s23177520

Song, Y., Zheng, Q., Liu, B., & Gao, X. (2023). EEG Conformer: Convolutional Transformer for EEG decoding and visualization. *IEEE Transactions on Neural Systems and Rehabilitation Engineering, 31, 710–719.* https://doi.org/10.1109/TNSRE.2022.3230250

Stam, C. J., Nolte, G., & Daffertshofer, A. (2007). Phase lag index: Assessment of functional connectivity from multichannel EEG and MEG with diminished bias from common sources. *Human Brain Mapping, 28(11), 1178–1193.* https://doi.org/10.1002/hbm.20346

Stam, C. J., & van Straaten, E. C. W. (2012). Go with the flow: Use of a directed phase lag index to characterize patterns of phase relations in a large-scale model of brain dynamics. *NeuroImage, 62(3), 1415–1428.* https://doi.org/10.1016/j.neuroimage.2012.05.050

Sun, Y., Chen, X., Liu, B., Liang, L., Wang, Y., Gao, S., & Gao, X. (2025). Signal acquisition of brain–computer interfaces: A medical–engineering crossover

perspective review. *Fundamental Research, 5(1), 3–16.* https://doi.org/10.1016/j.fmre.2024.04.011

Wang, K., Wang, Z., Guo, Y., He, F., Qi, H., Xu, M., & Ming, D. (2017). A brain–computer interface driven by imagining different force loads on a single hand: An online feasibility study. *Journal of NeuroEngineering and Rehabilitation, 14(1), Article 93.* https://doi.org/10.1186/s12984-017-0307-1

Yu, C., Dai, Y., & Liu, Y. (2025). Research progress of motor imagery-based brain–computer interface for upper limb rehabilitation. *Beijing Biomedical Engineering, 44(2), 198–204.*

Zhang, T., Liu, T., Li, F., Li, M., Liu, D., Zhang, R., He, H., Li, P., Gong, J., Luo, C., Yao, D., & Xu, P. (2016). Structural and functional correlates of motor imagery BCI performance: Insights from the patterns of fronto-parietal attention network. *NeuroImage, 134, 475–485.* https://doi.org/10.1016/j.neuroimage.2016.04.030

Zhao, L., Li, X., Bian, Y., Wang, X., & Yang, G. (2018). Study on feature modulation of electroencephalogram induced by motor imagery under multi-modal stimulation. *Journal of Biomedical Engineering, 35(3), 343–349.* https://doi.org/10.7507/1001-5515.201708061